

# Modelling the mechanics of 32 T REBCO superconductor magnet using numerical simulation

Arpit Kumar Srivastava\* & Enric Pardo<sup>†</sup>

Institute of Electrical Engineering, Slovak Academy of Sciences,  
Bratislava, Slovakia.

January 3, 2024

## Abstract

High temperature REBCO superconducting tapes are very promising for high-field magnets. With high magnetic field application there are high electro-mechanical forces, and thus concern for mechanical damage. Due to the presence of large screening currents and composite structure of the tape, the mechanical design of these magnets are not straight forward. In addition, many contemporary designs use insulated winding. In this work we develop a novel two-dimensional axisymmetric finite element tool programmed in MATLAB that assumes the displacement field within linear elastic range. The stack of pancakes and a large number of REBCO tape turns are approximated as an an-isotropic bulk hollow cylinder. Our results agree with uni-axial stress experiments in literature, validating the bulk approximation. Here, we study the following configuration. The current is first ramp up to below the critical current and we calculate the screening currents and the forces that they cause using the MEMEP model. This electromagnetic model can now take insulated magnets into account. As a case study, 32 T REBCO superconductor magnet, is taken and simulated numerically. We have done complete mechanical analysis of the magnet by including the axial and shear mechanical quantities for each pancake unlike previous work where only radial and circumferential quantities are focused. Effect on mechanical quantities without screening current is also calculated and compared. It is shown that including screening current induced field strongly affect the mechanical quantities, specially the shear stress. The latter might be the critical quantity for certain magnet configurations. Additionally, in order to overcome high stresses, a stiff over banding of different material is considered and numerically modelled which significantly reduces the mechanical stresses. The FE based model developed is efficient to calculate the mechanical behaviour of any general superconductor magnet and its devices.

*Keywords:* REBCO Superconductors, Screening current, Stress-strain analysis, high field magnet

## 1 Introduction

State of art high temperature superconducting REBCO tapes ( $REBa_2Cu_3O_{7-x}$ , where  $RE$  is a rare earth like Y, Gd or Sm) are promising candidates for the development of future high field magnets [1, 2].

---

\*arpit.srivastava@savba.sk

<sup>†</sup>enric.pardo@savba.sk

These high field applications include magnets for materials research [3–5], fusion reactors [6–8], particle accelerators [9–11] and medical equipments [12–15]. HTS windings has also been widely investigated to design electric air crafts [16–19]. The high field application require conductors with almost zero resistivity and extremely high current density [20]. In such high magnetic field application there are high electro-mechanical forces and thus concern for mechanical failure. In addition, screening current induced field [21] as well as an-isotropic and in-homogeneous [22] nature of REBCO tape altogether connive to complicate the mechanics of deformation very significantly. Therefore it is important to develop a numerical tool to quickly and efficiently analyze the distribution of stresses and strain in high field REBCO coils.

In recent years, a large number of numerical analyses are proposed to model the mechanics of REBCO superconductor coil insert for high field magnets. These works can be widely divided in two approaches. First approach for solving stress, strain and deformation is analytical as either in [23, 24] which is relatively straight forward where stresses are product of current density, coil radius and magnetic field or in [25] where a continuum model is proposed neglecting the height of coil assuming the problem as plane stress.

The other and mostly used approach is implementation of commercial software numerical model such as [26–33] and using transversely isotropic material properties for REBCO material.

Recently, based on aforementioned numerical model Trillaud *et al* [29] discussed about effect of mechanical degradation on critical current density  $J_c$ . In another study Xia *et al* [32] shows the effect of shielding current on high filed REBCO Coils. Ze Jing [30] explored about the effect of phase field magnetization assuming the magnet as bulk. In another work, Ueda *et al* [28] has shown the combined effect of cool down induced stresses and screening current on REBCO coil. A possibility of non circular pancake coils proposed by Wang *et al* [34] indicates that this design can prevent degradation in REBCO wire due to deformation.

In all the above study, subtle efforts have been made for mechanical modelling of REBCO coils on multi-physics software and couple it with electromagnetic forces in either sequential or iterative manner.

Apart from the issue to solve this multiphysics problem numerically, for the safe design of high field magnet and devices, generation of screening current induced field (SCIF) [35], is a challenge as it affects not only the mechanical behaviour [36] but also homogeneity of the field [35, 37].

To the best of our knowledge, there has not yet been a comprehensive study to solve mechanical equilibrium equations for an-isotropic REBCO superconductors magnet with SCIF and overbanding using finite element analysis. Recently, Yufan yan *et al* [38] also discussed about impact of screening current and overbanding on REBCO magnets but the study limited to circumferential stresses and strains.

In this study, we have developed a finite element scheme to study screening current induced stresses and strains in a high temperature axis-symmetric superconductor REBCO insert pancake coils. The strains are considered in linear elastic range for the current study. This is a reasonable assumption as for fail safe design of high field superconductor magnet firstly because the mechanical deformation should be in the range of reversible elastic range so that tapes are not degraded [39] and secondly as the REBCO material is highly brittle [40] in nature. The finite element (FE) code is developed in MATLAB and coupled to already developed MEMEP model [35, 41]. We rely on homogenization approach to deal with anisotropic nature of HTS tapes [32, 42].

The paper is organized as follows. In Section 2, the HTS insert geometrical and input parameters are described. In section 3, we have discussed the numerical model used to develop the computational framework to study the electro-mechanical analysis.

First, we present the electromagnetic model based on variational principles that calculates the screening currents and Lorentz forces. Later, we discuss the electromechanical model for axi-symmetric magnet geometry. A numerical fit shows the validation of bulk approximation with experimental uniaxial stress-strain. In that section, we introduce overbanding and the numerical scheme to handle its mechanics.

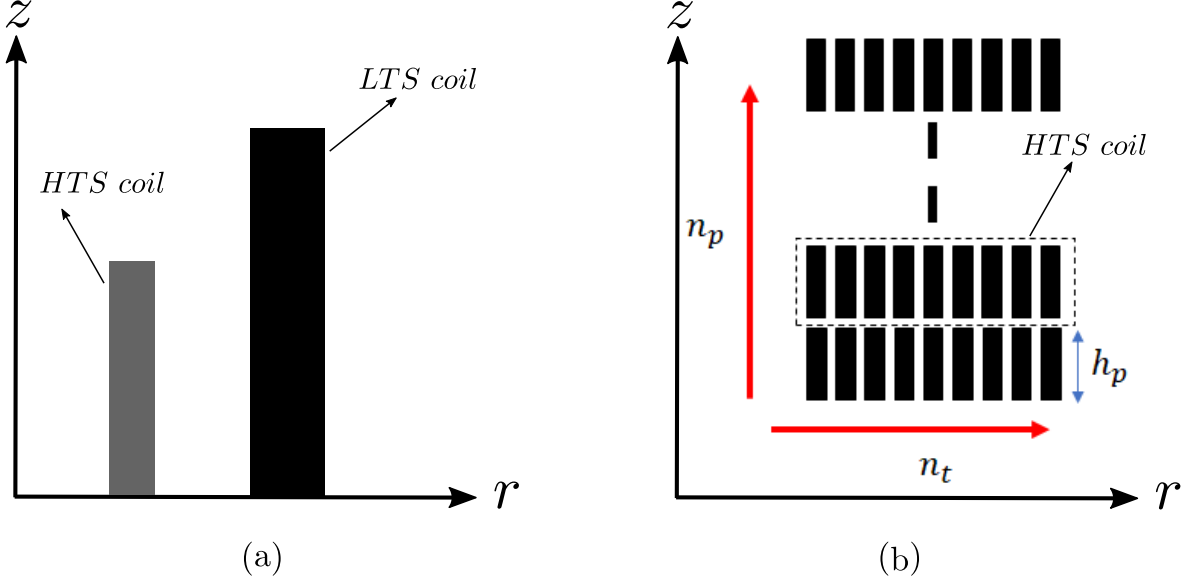


Figure 1: (a) Schematic of an Axis-symmetric REBCO Superconductor magnet in quarter  $r$ - $z$  plane and (b) HTS coil magnet with number of pancakes  $n_p$  in  $z$  direction and number of turns  $n_t$  in radial direction. The height of each pancake is  $h_p$ .

Section 4 presents computation of mechanical properties with and without screening current and effect of overbanding for a 32T magnet.

## 2 HTS magnet insert

An 8 double-pancake REBCO insert for a 32 T superconductor magnet is chosen as an example to implement mechanical properties. The REBCO insert is used in conjunction with LTS outer magnet which provide 19 T background field at the bore center. The magnet geometry and properties is given in figure 1 and table 1.

The REBCO insert design is for a metal-insulated coil, where a stainless-steel (SS) tape is co-wound with the superconductor. Taking into account, the high turn-to-turn surface resistance through the SS (around  $10^{-6} - 10^{-7} \Omega\text{m}^2$ ), the radial currents can be neglected [43]

The elastic and geometric properties are listed in table 2.

## 3 Numerical model

### 3.1 Electromagnetic model

In this work, we compute the local current density taking screening currents into account by the Minimum Electro-Magnetic Entropy Production (MEMEP), as described in [35, 41, 43]. For simplicity, we assume

32 T magnet coil geometry	
Parameter	Value
$R_{in}$	25 mm
$R_{out}$	56.5 mm
Number of double pancake ( $n_p$ )	8
Number of turn in each pancake ( $n_t$ )	250
thickness of each tape layer	105 $\mu m$
Height of pancake coil ( $h_p$ )	6 mm

Table 1: Parameters used for REBCO insert magnet.

Material properties of tape at 4.2 K [32]			
Component	$E$ (GPa)	$\nu$	t ( $\mu m$ )
REBCO	180	0.3	1
Hastealloy	210	0.3	80
Copper	40	0.3	20
Ag+Buffer	90	0.3	2
SS tape	156	0.3	2

Table 2: Material properties for REBCO tapes.

axi-symmetrical geometry for the pancake coils (see, figure 2), which is justified because the tape and insulation thickness is much smaller than the coil inner radius.

Regarding the electromagnetic properties, we assume that the superconducting layer presents a power-law relation between the electric field,  $\mathbf{E}$ , and the current density  $\mathbf{J}$  as

$$\mathbf{E}(\mathbf{J}) = E_c \left( \frac{|\mathbf{J}|}{J_c} \right)^n \frac{\mathbf{J}}{|\mathbf{J}|}, \quad (1)$$

where  $E_c = 10^{-4}$  V/m,  $J_c$  is the critical current density, and  $n$  is the power-law exponent. In this article, we assume that  $n$  is constant with value 30 and  $J_c$  depends on the magnetic field and its orientation,  $J_c(B, \theta)$ . As input, we use  $J_c(B, \theta)$  according to the analytical fit of experimental data in [44] for a Fujikura tape. We also consider the resistance of the metal stabilization, substrate and isolation by taking a homogenized anisotropic resistance into account, as in [43].

In this work, we consider that the radial turn-to-turn resistance is very high, and hence we assume that this resistance is infinite. In order to speed-up the computations, we group several turns in a single element in the radial direction (10 turns in this case).

In our model, we consider the realistic background magnetic field,  $\mathbf{B}_a$ , created by the low-temperature superconducting (LTS) outsert, which we compute from the actual cross-section of the LTS winding and the Biot-Savart law. The generated magnetic field from the LTS at the bore center, as well as most of the HTS insert, is 19 T.

Once MEMEP finds both local current density and the magnetic field, the Lorenz force density is computed as

$$\mathbf{f}_L = \mathbf{J} \times \mathbf{B} \quad (2)$$

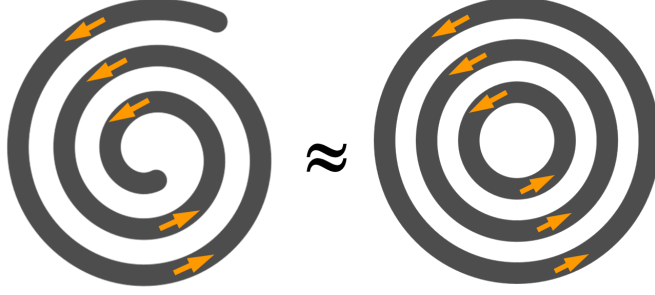


Figure 2: Spiral geometry of REBCO Superconductor coil winding and approximated as closely packed co-centric circular geometry. The arrow denotes the direction of flow of current for an insulated case.

and in expanded general form

$$\mathbf{f}_L = f_r \mathbf{e}_r + f_\phi \mathbf{e}_\phi + f_z \mathbf{e}_z, \quad (3)$$

where  $\mathbf{e}_r$ ,  $\mathbf{e}_\phi$  and  $\mathbf{e}_z$  are the unit vectors in radial, circumferential and axial directions and the components of the force density are  $f_r = J_\phi B_z - J_z B_\phi$ ,  $f_\phi = J_z B_r - J_r B_z$  and  $f_z = J_r B_\phi - J_\phi B_r$ . For isolated windings,  $J_r$  vanishes and for tape an isolation thickness much lower than the inner radius,  $J_z$  is negligible compared to  $J_\phi$ . Then, only  $J_\phi$  is relevant, and hence

$$\mathbf{f}_L = J_\phi B_z \mathbf{e}_r - J_\phi B_r \mathbf{e}_z. \quad (4)$$

As shown in [43], the radial currents are negligible in metal-insulated magnets under regular operation. Thus, we can assume that the Lorentz forces in metal-insulated magnets is the same as in insulated.

### 3.2 Electro-mechanical model

For the case study of magnet and developing the tool, the following assumption are made

1. Thermal stresses are neglected.
2. There is no sliding between the turns, they are perfectly bonded to each other.
3. Residual stresses due to winding tension are neglected.

The assumption of coil turns of REBCO HTS into concentric coils simplified the problem domain to study the problem as axi-symmetry. In this study, each pancake is assumed as axi-symmetric hollow ring (see, [35]) and the corresponding stresses and strains are calculated. We deal the an-isotropic material properties of the tape with an analogous bulk model (see section 3.2.1). We start with the general deformation field given as,

$$\mathbf{u} = u_r \mathbf{e}_r + u_\phi \mathbf{e}_\phi + u_z \mathbf{e}_z \quad (5)$$

and the corresponding strain tensor field is given by

$$\boldsymbol{\epsilon} = \frac{1}{2} [\boldsymbol{\nabla} \mathbf{u} + \boldsymbol{\nabla} \mathbf{u}^T] \quad (6)$$

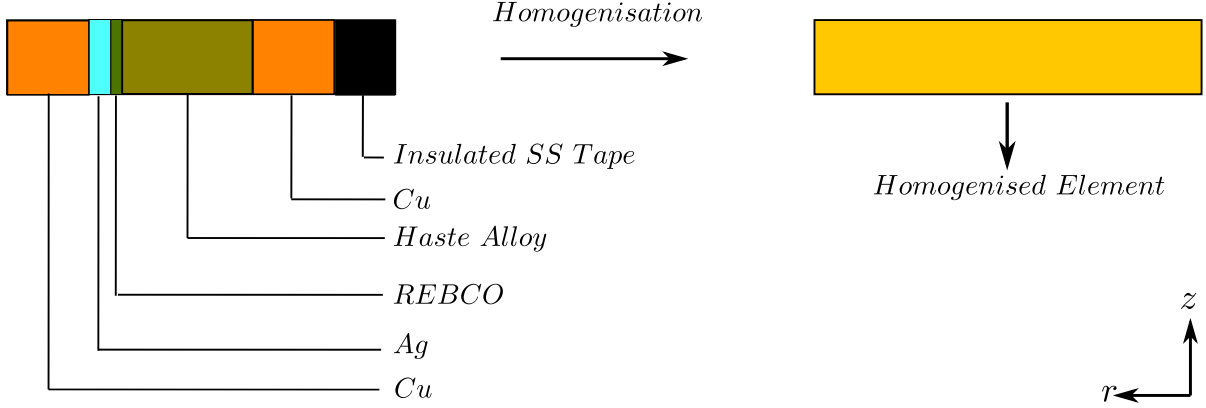


Figure 3: Schematic of tape layered structure and homogenised RVE of a single tape in r-z plane.

due to axis-symmetry and the fact that circumferential displacement is independent of  $\phi$  co-ordinate, the only strain components are

$$\epsilon_r = \frac{\partial u_r}{\partial r}, \epsilon_\phi = \frac{u_r}{r}, \epsilon_z = \frac{\partial u_z}{\partial z}, \epsilon_{rz} = \frac{1}{2} \left( \frac{\partial u_r}{\partial z} + \frac{\partial u_z}{\partial r} \right) \quad (7)$$

Assuming the material within the range of linear elastic limit, the consistence stresses are related to strains by constitutive relationship given as:

$$\boldsymbol{\sigma} = D\boldsymbol{\epsilon} \quad (8)$$

where  $D$  is the elasticity matrix, which presents anisotropic material properties due to the laminated structure of tape [45]. A bulk homogenization approach is used to calculate the components of elasticity matrix whose details are given in section 3.2.1. From the basic continuum mechanics the equilibrium equation for a body subjected to only body forces  $\mathbf{f}_b$  is given by

$$\nabla \cdot \boldsymbol{\sigma} + \mathbf{f}_b = 0 \quad (9)$$

Due to axis-symmetry geometry, the only stress components are  $\sigma_r$ ,  $\sigma_\phi$ ,  $\sigma_z$  and  $\sigma_{rz}$  and the governing equations are given by

$$\begin{aligned} \frac{\partial \sigma_r}{\partial r} + \frac{\partial \sigma_{rz}}{\partial z} + \frac{\sigma_r - \sigma_\phi}{r} + f_r &= 0, \\ \frac{\partial \sigma_{rz}}{\partial r} + \frac{\partial \sigma_z}{\partial z} + \frac{\sigma_{rz}}{r} + f_z &= 0 \end{aligned} \quad (10)$$

where  $f_r$  and  $f_z$  are body forces due to electro-mechanical Lorentz force in radial and axial directions respectively.

### 3.2.1 Homogenized Element

: In this section, the anisotropy of the tape structure is dealt in a similar way as explained in [32]. This approach is known as bulk approximation and widely used assuming the laminated pancake as

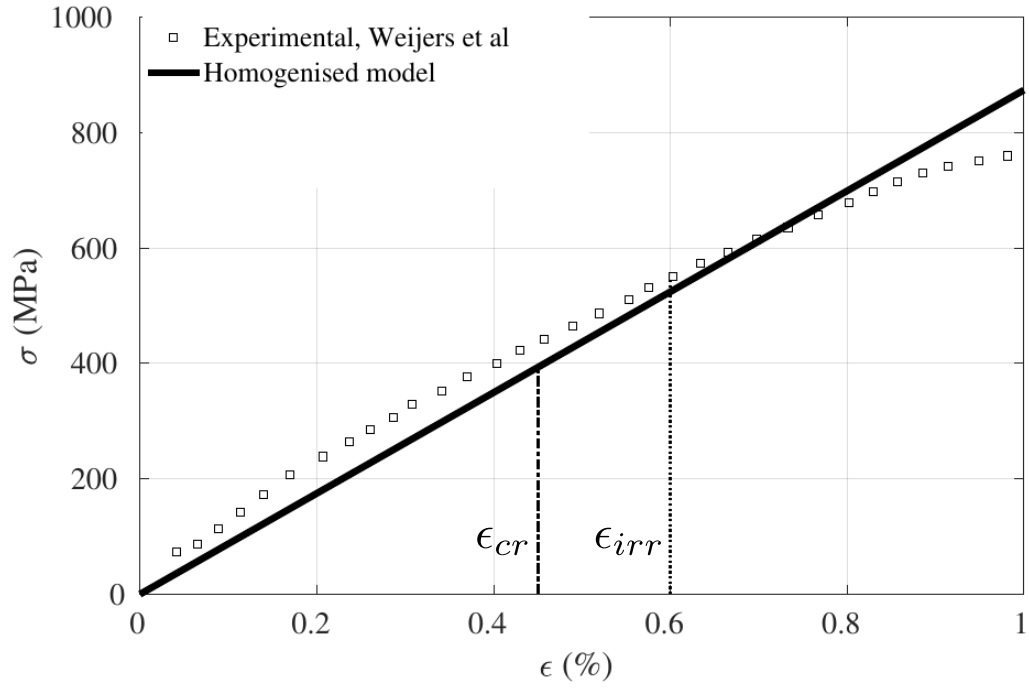


Figure 4: Homogenised model compared with experimental stress strain of REBCO Superconductor [46]. The dash-dot vertical lines are correspond to  $\epsilon_{cr} = 0.45\%$  below which critical current density  $J_c$  of the tape is almost constant and  $\epsilon_{irr} = 0.6\%$  [47] beyond which there is plastic deformation and critical current density  $J_c$  will permanently degraded.

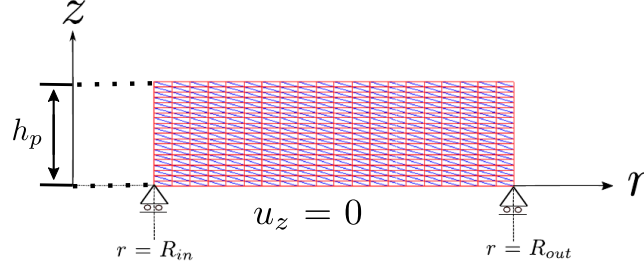


Figure 5: A typical mesh of a pancake with triangular element. Each pancake in HTS magnet is subjected to roller boundary condition i.e. axial displacement  $u_z = 0$  on bottom of each pancake.

a continuum disk. The equivalent homogeneous representative volume element (RVE) have isotropic property in the  $\phi - z$  plane (see, figure 3) and different in radial direction. Further, the transversely isotropic elasticity matrix  $D$  which relate axis symmetric stresses with corresponding strains is given by

$$\begin{bmatrix} \sigma_r \\ \sigma_\phi \\ \sigma_z \\ \sigma_{rz} \end{bmatrix} = \begin{bmatrix} D_{11} & D_{12} & D_{12} & 0 \\ D_{12} & D_{22} & D_{23} & 0 \\ D_{12} & D_{23} & D_{22} & 0 \\ 0 & 0 & 0 & D_{44} \end{bmatrix} \begin{bmatrix} \epsilon_r \\ \epsilon_\phi \\ \epsilon_z \\ \epsilon_{rz} \end{bmatrix} \quad (11)$$

The components of the  $D$  matrix are a function of the Elastic modulus  $\bar{E}$ , Poisson's ratio  $\bar{\nu}$  and thickness of each layer of laminated tape  $t_m$  and calculated following [45]. The homogenised material properties are given as following

$$\begin{aligned} D_{11} = \bar{E}_r &= \frac{1}{\sum_{m=1}^n t_m / E_m} \\ D_{22} = \bar{E}_\phi = \bar{E}_z &= \sum_{m=1}^n t_m E_m \\ \bar{\nu}_{\phi z} &= \frac{\sum_{m=1}^n t_m \nu_m E_m}{\sum_{m=1}^n t_m E_m}, \bar{\nu}_{rz} = \frac{\bar{E}_r}{\bar{E}_z} \sum_{m=1}^n t_m E_m \\ D_{12} = D_{44} &= \bar{\nu}_{rz} \bar{E}_r, D_{23} = \bar{\nu}_{\phi z} \bar{E}_\phi \end{aligned} \quad (12)$$

where  $n$  is number of laminated layer in REBCO tape,  $E_m$  and  $t_m$  are modulus of elasticity and thickness of the tape layer respectively.

We then calculated the  $\bar{E}$  matrix from  $E_m$  and  $\nu_m$  experimentally obtained in [46]. Clearly the model is able to capture the uni-axial stress-strain response as shown in figure 4. At this stage it is more appropriate to say that with in elastic range as shown in figure 4 the model response is quite good.

### 3.2.2 Finite Element Implementation

: In this section we closely follow finite element formulation as in [48] for axis-symmetry space to obtain mechanical stress and strain for REBCO tapes subjected to electromechanical forces. The charging



process of the magnet is assumed very slow so that inertia effects can be neglected. In general finite element approach, the global stiffness  $K_G$ , nodal displacements and global nodal forces  $F_G$  are related as

$$[K_G][U] = [F_G] \quad (13)$$

in an element they follow

$$[K_e][U_e] = [F_e] \quad (14)$$

where  $K_e$ ,  $U_e$  and  $F_e$  are element stiffness, nodal displacement and nodal forces in the element, respectively.

Next we briefly discuss on finding the element stiffness and subsequently global displacement for the problem which is well defined (see [48] for detail). First we define radial and axial displacement field  $u_r$  and  $u_z$  which are given by in discretized form as

$$\begin{aligned} u_r &= \sum_{i=1}^{n_e} N_i U_{r_i} \\ u_z &= \sum_{i=1}^{n_e} N_i U_{z_i} \end{aligned} \quad (15)$$

where  $n_e$  is the number of node where  $u_r$  and  $u_z$  are calculated in an element and  $N_i$  are shape functions. Though shape functions depend on the choice of element shape, general procedure will remain as same.

For the present study we have discretized the pancake domain in triangular elements as shown in figure 5. The  $U_{r_i}$  and  $U_{z_i}$  are the radial and axial displacement of  $i_{th}$  node respectively. Assuming triangular elements with node indexes  $i, j, k$ , the axis-symmetric strains in each element are given by

$$\begin{bmatrix} \epsilon_r \\ \epsilon_\phi \\ \epsilon_z \\ \epsilon_{rz} \end{bmatrix} = \begin{bmatrix} \frac{\partial N_i}{\partial r} & 0 & \frac{\partial N_j}{\partial r} & 0 & \frac{\partial N_m}{\partial r} & 0 \\ \frac{N_i}{r} & 0 & \frac{N_j}{r} & 0 & \frac{N_m}{r} & 0 \\ 0 & \frac{\partial N_i}{\partial z} & 0 & \frac{\partial N_j}{\partial z} & 0 & \frac{\partial N_m}{\partial z} \\ \frac{\partial N_i}{\partial z} & \frac{\partial N_i}{\partial r} & \frac{\partial N_j}{\partial z} & \frac{\partial N_j}{\partial r} & \frac{\partial N_m}{\partial z} & \frac{\partial N_m}{\partial r} \end{bmatrix} \begin{bmatrix} U_{r_i} \\ U_{z_i} \\ U_{r_j} \\ U_{z_j} \\ U_{r_m} \\ U_{z_m} \end{bmatrix}, \quad (16)$$

which can be written as

$$[\epsilon_e] = [B][U_e] \quad (17)$$

where the components of B are differential of shape function of the element and refer as the geometric stiffness as it depend on geometric parameters and it relates the strain with the displacement.

Using equation (8), elemental stresses are calculated as

$$[\sigma_e] = [D][B][U_e] \quad (18)$$

The strain energy due to deformation in an element is given by,

$$W_{int} = \frac{1}{2} \int_{v_e} \boldsymbol{\sigma} \cdot \boldsymbol{\epsilon} dv \quad (19)$$

Hence,

$$W_{int} = \frac{1}{2} [U_e]^T \left[ \int_{v_e} [B]^T [D] [B] dv \right] [U_e] \quad (20)$$

In the finite element set up for solid materials the elemental stiffness  $K_e$  is given by

$$K_e = \int_{v_e} [B]^T [D] [B] dv \quad (21)$$

which can be modified for the axis symmetric case as

$$K_e = 2\pi \int_{dA_e} [B]^T [D] [B] r dr dz \quad (22)$$

and further can be approximated as

$$K_e = 2\pi \bar{r}_e A_e [\bar{B}]^T [D] [\bar{B}] \quad (23)$$

where  $\bar{r}_e$  is radial coordinate of centroid of element and  $\bar{B}$  are calculated at centroid of element.  $A_e$  is the cross section area of element. The global stiffness  $K_G$  is now calculated using component of elemental stiffness  $K_e$ .

Now to calculate forces which for the present situation is only body forces and obtained as explained in section 3.2. Following finite element setup as explained in [48]

For small element size, the force vector at  $i_{th}$  node is

$$F_i = \frac{2}{3} \pi \bar{r}_e A_e [f_L]$$

and in elemental

$$[F_e] = \begin{bmatrix} F_i \\ F_j \\ F_k \end{bmatrix} \quad (24)$$

where  $f_L$  is lorentz forces density whose components are obtained from equation (4). Each node has two degree of freedom in radial and axial direction respectively. The corresponding global force  $F_G$  then can be calculated using elemental forces  $F_e$ .

At this stage, deformation or forces at the nodes can be calculated using global displacement and force relation (see, equation 13). Also, since we are using first order triangular element so number of integration point is only the centroid of the triangle and strains as well as stresses are calculated at this integration point.

### 3.2.3 Overbanding Stiffness

:

It is important to discuss the inclusion of stiffness property of the overbanding as shown in figure 6 for the problem at this stage. For the numerical analysis, the following assumption are made

1. The overbanding turns are considered as continuum bulk.
2. The adjacent overbanding turn are perfectly bonded to each other.
3. The junction of superconductor tape and overbanding material share common boundary and are perfectly bonded to each other.

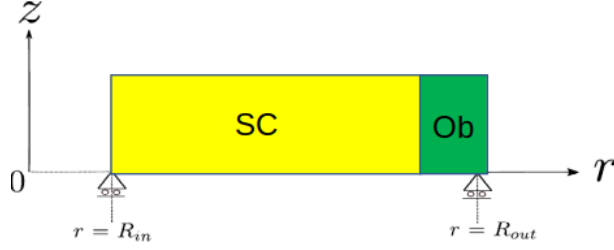


Figure 6: A schematic of pancake with over banding layers subjected to roller boundary condition in  $r - z$  plane

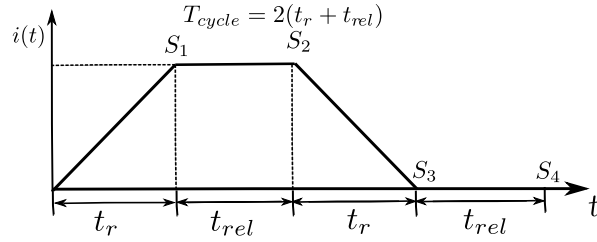


Figure 7: A Cycle of input current in a magnet used for charging and discharging the magnet. First the current is ramp up to  $I_{max}$  corresponding to  $S_1$  and till point  $S_2$  this  $I_{max}$  is kept constant. The current is then ramped down to zero during  $S_2$  and  $S_3$  and in this zero state for interval  $S_3$  and  $S_4$ .

These assumptions do not enable slip between the two different materials: superconducting coil and overbanding.

The pancake is discretized in triangular elements as shown in figure 5. Now if total number of node in the superconducting material are  $n_{t_{sc}}$  and total number of nodes in whole domain are  $n_t$ .

If value all the three nodes of the element is less than  $n_{t_{sc}}$ , the elemental stiffness for the triangular element is given by,

$$K_e = 2\pi\bar{r}_e A_e [\bar{B}^T] [D_{sc}] [\bar{B}],$$

otherwise

$$K_e = 2\pi\bar{r}_e A_e [\bar{B}^T] [D_{ob}] [\bar{B}] \quad (25)$$

where  $D_{sc}$  and  $D_{ob}$  are material properties for REBCO superconductor and overbanding material respectively.

## 4 Results

The numerical model developed in section 3.2.2 is implemented to investigate the mechanical properties of the 32 T REBCO superconductor HTS magnet as explained in section 3.2.

where,  $t_r$  is the ramp up as well ramp down charging time. The ramp down discharging time is also same. The relaxation time after charging and discharging is  $t_{rel}$ . Then, the total time for one cycle is  $T = 2(t_r + t_{rel})$ . For the current analysis  $t_r = t_{rel} = 333$  s and  $I_{max} = 333$  A. Hence, the rate of ramp is 1 A/s.

## 4.1 Electromagnetic analysis

In this section, we have done electromagnetic analysis using the inputs defined in section 2 and using the coil geometry given in table 1. First, we discuss the initial ramp (figure 8(a-d)). The circumferential current density  $J_\phi$  is shown for each pancake at every quarter of ramp time  $t_r$ . Initially, at low current the current density is uniform and low in all pancakes, except a narrow layer close to the top and bottom of each pancake but as we increase the  $I$ , the current density is high in most of the pancakes cross-section, specially in the upper and lower pancakes. This is due to time-varying magnetic field in the radial direction. Initially, for  $t \leq t_r/2$ , the current density is roughly anti-symmetric with respect to the center of each pancake cross-section.

The magnet is subjected to constant current and then it is decreased in discharging process. The current density for these cases are in figures 8(e) and 8(f), respectively. In the latter, the current density is purely due to screening currents.

The axial magnetic field is shown for the same process in figure 9. The field monotonically decreases with the radius. Also, the maximum magnetic field, of around 32 T, is at the inner radius of the central pancakes.

Figure 10(a-e) shows the radial Lorentz force density. Screening current effect can be easily seen as pancakes farther from center experience positive and negative radial forces within the same pancake. The magnitude of maximum force density is  $6 \times 10^{10}$  N/m<sup>3</sup>. We have also analyzed the force in the magnet at the end of the ramp when there is no screening current (see, figure 10(f)). Clearly, forces are all positive, as well as more uniform and lower than for the case without screening current, reaching a maximum value 3 times lower than when screening currents are taken into account. The lower value of the force is due to lower local current density.

The axial forces in the magnet are much lower ( $\approx \frac{1}{10}$  times) than radial forces, and hence they effectively do not contribute to magnet mechanics. This is due to the fact that the axial magnetic field  $B_z$  is much greater than the radial magnetic field  $B_r$ .

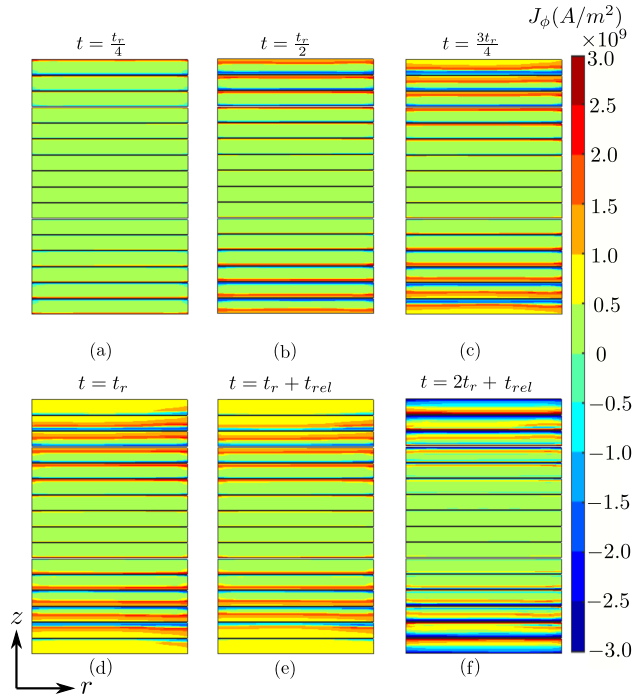


Figure 8: Variation of circumferential current density  $J_\phi$  in a cycle for the whole magnet with screening current induced field. (a) to (c) is charging, (d) fully charged state, (e) discharged state and (f) discharged state with relaxation time  $t_{rel}$ .

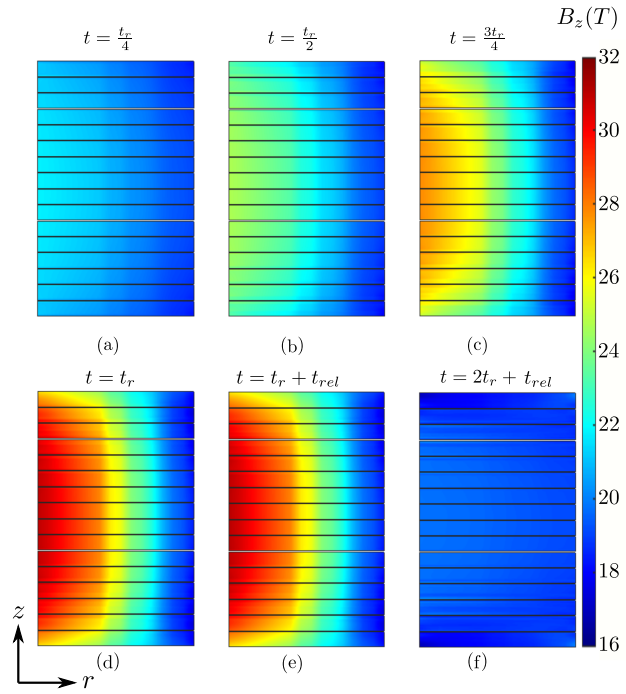


Figure 9: Variation of axial magnetic field  $B_z$  in a cycle for the whole magnet with screening current induced field. (a) to (c) Charging, (d) fully charged state, (e) discharged state and (f) discharged state with relaxation time  $t_{rel}$ .

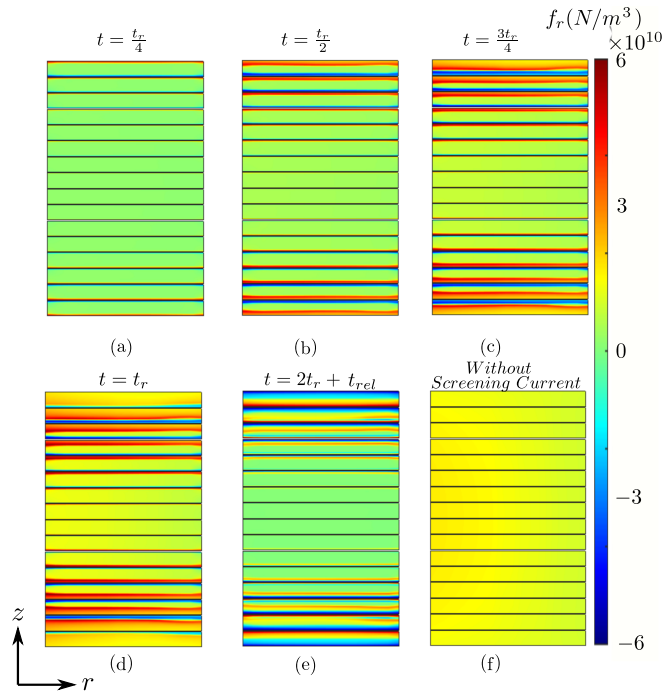


Figure 10: Variation of radial force in a cycle for the whole magnet with screening current induced field. (a) to (c) is charging, (d) fully charged state, (e) discharged state and (f) without Screening current.

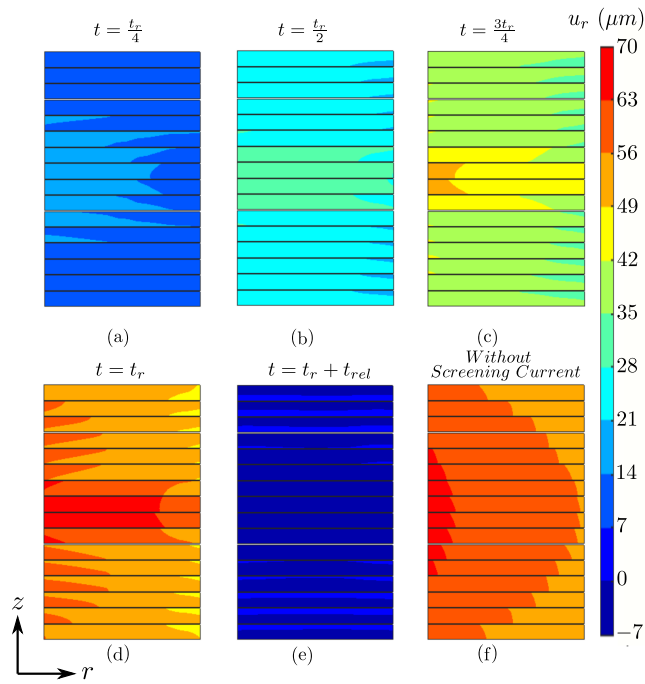


Figure 11: Variation of radial displacement  $u_r$  in a cycle for the whole magnet with screening current induced field. (a) to (c) Charging, (d) fully charged state, (e) discharged state and (f) without Screening current.



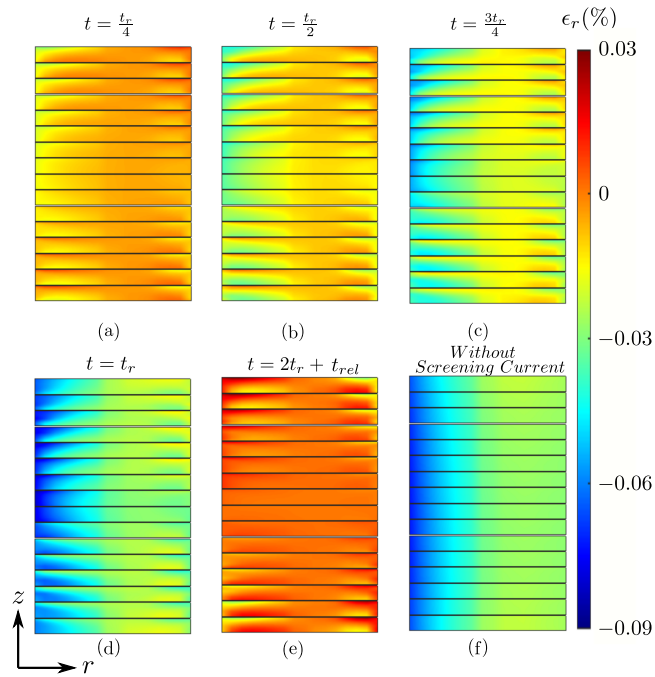


Figure 12: Variation of radial strain  $\epsilon_r$  in a cycle for the whole magnet with screening current induced field. (a) to (c) Charging, (d) fully charged state, (e) discharged state and (f) without Screening current.

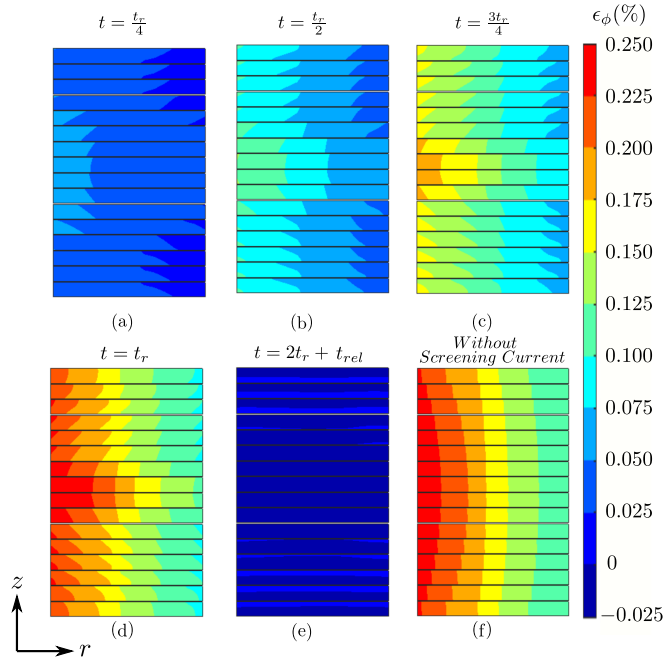


Figure 13: Variation of circumferential strain  $\epsilon_\phi$  in a cycle for the whole magnet with screening current induced field. (a) to (c) Charging, (d) fully charged state, (e) discharged state and (f) without Screening current.

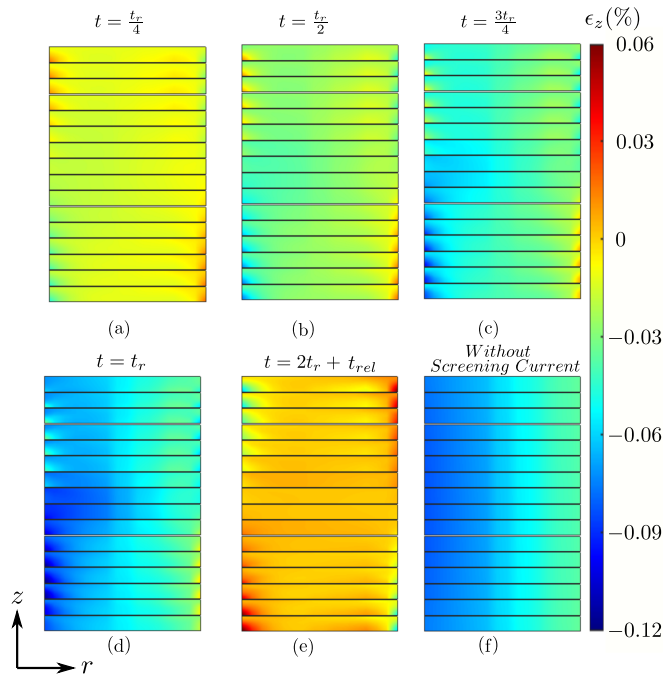


Figure 14: Variation of axial strain  $\epsilon_z$  in a cycle for the whole magnet with screening current induced field. (a) to (c) Charging, (d) fully charged state, (e) discharged state and (f) without Screening current.

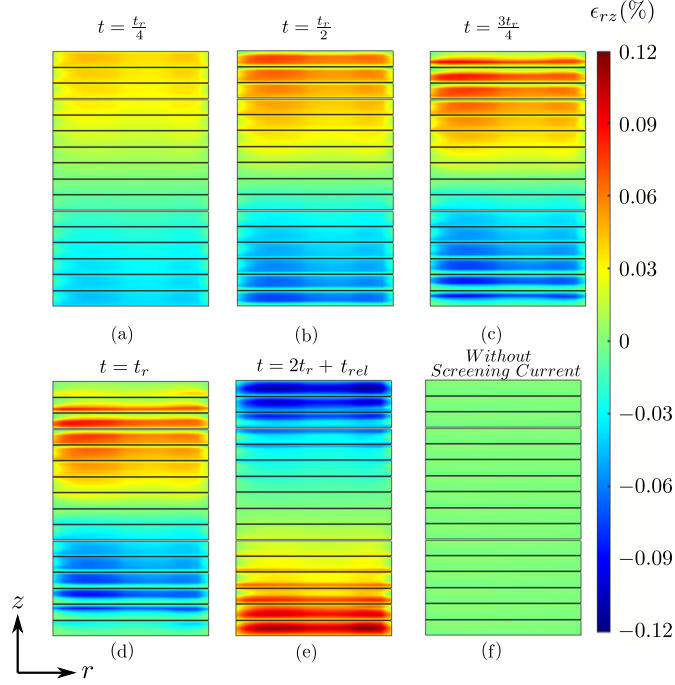


Figure 15: Variation of shear strain  $\epsilon_{rz}$  in a cycle for the whole magnet with screening current induced field. (a) to (c) Charging, (d) fully charged state, (e) discharged state and (f) without Screening current.

## 4.2 Mechanical properties with and without Screening current

We now import forces to the finite element model to further calculate the mechanical quantities in sequential manner.

### 4.2.1 Displacement and strain fields in magnet:

First, we calculate the radial displacement (see, figure 11). The maximum displacement occurs at the maximum current and at center of the pancakes in magnet because the radial forces there are all positive (see, figure 10(d)), and hence these forces are pushing the superconductor radially outwards. The maximum magnitude of displacement is only  $70 \mu\text{m}$ . Till this point, the displacement is radially outward only. Interestingly, when the current is ramped down in discharged state (see, figure 11(e)), the deformation field is highly non homogeneous due to forces that are also non-uniform because of the screening currents. If we observe the top of the pancake at the outermost diameter, the deformation is negative and positive, that is on the edges the deformation is not uniform.

The displacement field when there is no screening current is maximum at the center (figure 11(f)). The comparison of the two cases clearly shows that the maximum displacement is highly non-uniform in the magnet subjected to SCIF.

Figures 12-14 show the radial, circumferential and axial strain in the magnet.

The radial strain field is compressive in nature while charging, whether screening current is considered or not. The maximum magnitude of radial strain is 0.09 % when the magnet is fully charged. The

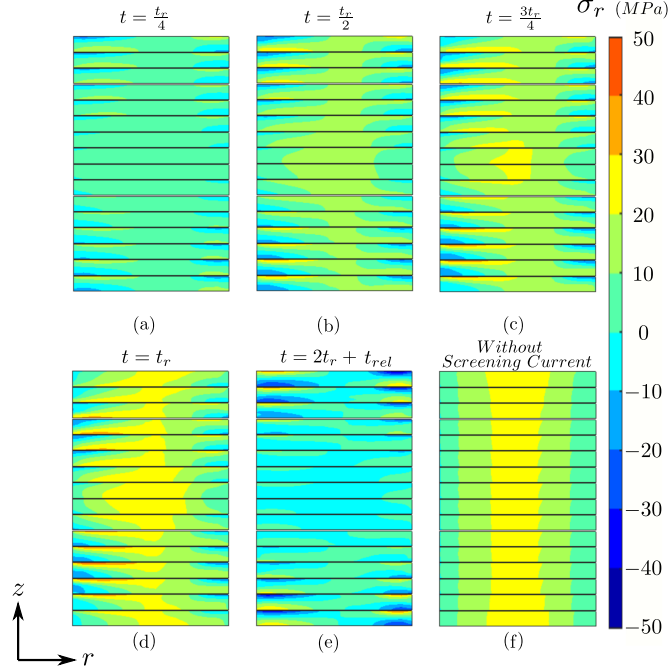


Figure 16: Evolution of Radial Stress  $\sigma_r$  in a cycle for the whole magnet with screening current induced field. (a) to (c) Charging, (d) fully charged state, (e) discharged state and (f) without Screening current.

maximum strain appears in the central pancakes (see figure 12(d)). For the pancakes farther from the center, one may clearly see that the edges are subjected to non uniform radial strain due to SCIF. At fully discharged state  $\epsilon_r$  is both tensile and compressive mostly in the top and bottom pancakes (see figure 12(e)). The variation is from tensile  $+0.03\%$  to compressive  $-0.03\%$  within the pancake. For no screening currents at the end of the ramp, the radial currents are more homogeneous (figure 12(f)).

The evolution of circumferential strain for the charging and discharging cycle is shown in figure 13. In agreement with literature [38, 49], the circumferential strain is maximum among all the other strain and should be of concern. For the present analysis the maximum circumferential strain is at the inner radius of the central pancakes. The order of  $\epsilon_\phi$  is around  $0.25\%$  which is in line with our assumption that critical current density is independent of deformation.

The calculation, taking SCIF into account, does not highly change the results. However, assuming uniform current density results in more uniform  $\epsilon_\phi$  (see, figure 13(f)). After discharging, the circumferential strain is both tensile and compressive. This is due to the fact that this only depends on the radial displacement and the displacement is positive and negative (see figure 11(e)) with in the pancake.

We also calculate the axial strain (see, figure 14). Curiously, the axial strain does not vanish, in spite of the fact that we neglect axial Lorentz forces. While charging, the axial strain in each pancake is compressive in most of its cross section (see figure 14(d)). Due to the screening currents and the forces that they create, the sign of  $\epsilon_z$  is anti-symmetric with respect to the center of the coil cross-section. This is due to the symmetry of the Lorentz force caused by the screening currents. The maximum magnitude of axial strain is at fully charged state is  $0.12\%$  and compressive in nature, which appears

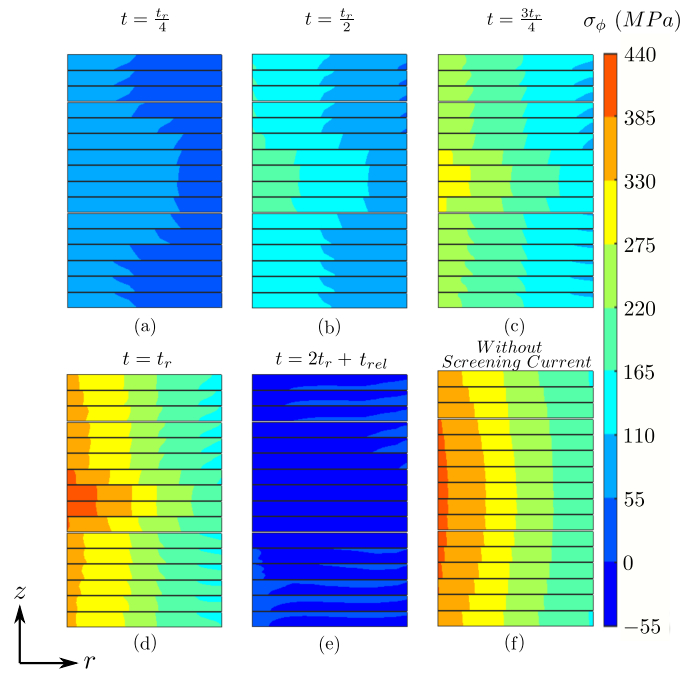


Figure 17: Variation of circumferential stress  $\sigma_\phi$  in a cycle for the whole magnet with screening current induced field. (a) to (c) Charging, (d) fully charged state, (e) discharged state and (f) without Screening current.

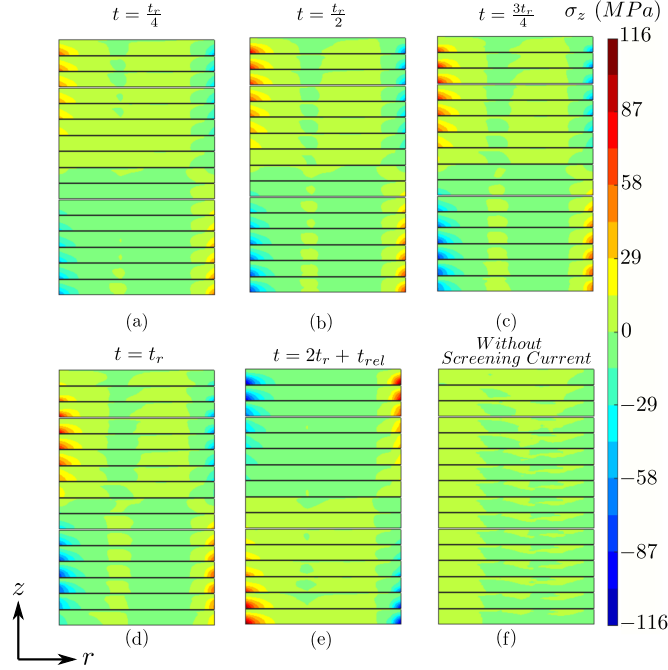


Figure 18: Variation of axial stress  $\sigma_z$  in a cycle for the whole magnet with screening current induced field. (a) to (c) Charging, (d) fully charged state, (e) discharged state and (f) without Screening current.

at the central pancakes. The axial strains are more non homogeneous at the fully discharged state, as shown in figure 14(e). Again, when there is no screening current the magnitude of axial strain is lower, which is now always compressive(see figure 14(f)).

Figure 15 shows the shear strain in all the pancakes of the magnet. The shear effect only appears in the cases where SCIF is considered. The top half of the winding experiences positive shear while at the bottom opposite to it. The magnitude of maximum shear strain is around 0.09 %.

Interestingly, the shear changes its nature while discharging: the upper half of the whole winding experiences negative shear, being opposite at the bottom half. In addition, the magnitude increases to 0.12 % even at zero current.

When there is no screening current there is negligible shear as current density, and hence forces, are more uniform, see figure 15(f).

#### 4.2.2 Stress field in magnet:

Radial stresses for the magnet are plotted in figure 16. The radial stresses are increasing as the current is increasing. Due to non uniform screening currents each pancakes in the magnet is subjected to compressive and tensile stresses within the pancakes except in the central pancakes, where radial stresses are only tensile. This is due to the fact that central pancakes are subjected to more uniform Lorentz force density (see, figure 10(d)).

When the magnet is fully charged, the maximum stress is 50 MPa while the minimum is  $-25$  MPa. In fully discharged state the stresses are low in most region of magnet pancakes except around edges where

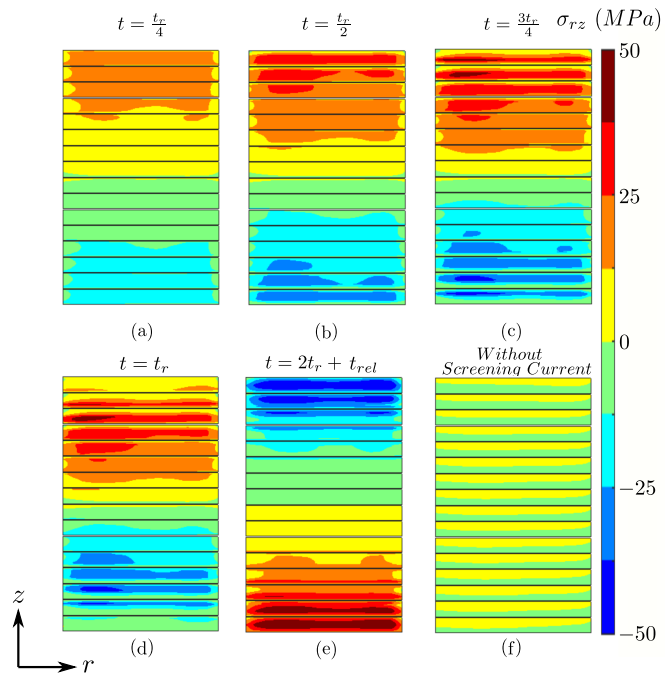


Figure 19: Variation of shear stress  $\sigma_{rz}$  in a cycle for the whole magnet with screening current induced field. (a) to (c) Charging, (d) fully charged state, (e) discharged state and (f) without Screening current.



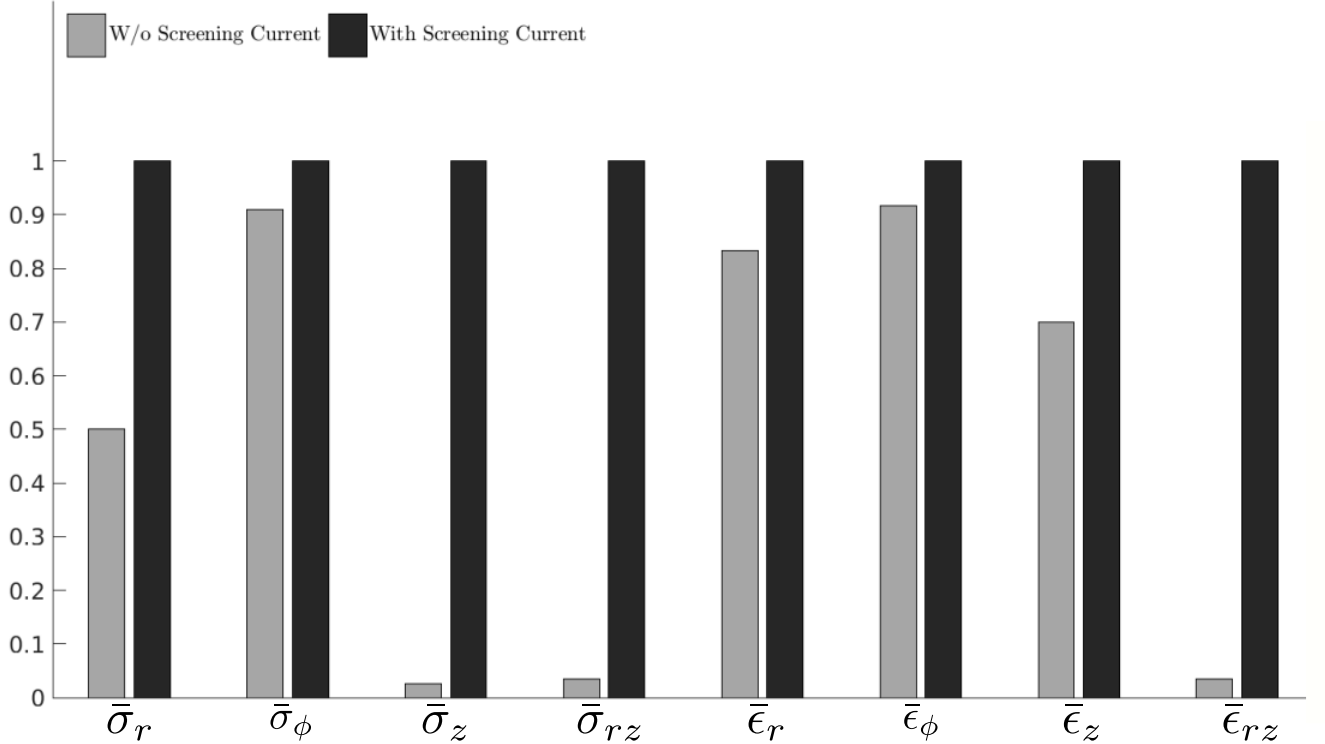


Figure 20: Comparison of mechanical quantities for magnet with and without screening current induced field.

it ranges from 50 MPa to  $-50$  MPa (see, figure 16(e)). In addition, the radial stresses are opposite in sign close to the top and bottom of each pancake because the Lorentz forces (and current density) are also opposite in sign.

Figure16(f) shows the distribution of radial stress for the case where there is no screening current. Now, the radial stresses are positive across the whole magnet. The maximum radial stresses are reduced to around 50 % compared to the radial stresses in case with screening current for same input current and magnet geometry. Also, tensile radial stress is undesirable for design point of view, since all turns should be in physical contact with each other in a non-impregnated winding. Therefore, radial stress should be compressive at least in part of the tape width in order to enable physical contact between tapes. Otherwise, radial tensile stress could detach the tapes from each other in the radial direction. If detachment occurs, it will worsen the average thermal conductivity in the radial direction. In addition, the radial electric resistance will dramatically increase, which could be an issue for electro-thermal stability .

In a soldered or impregnated winding, sufficiently large tensile stress could delaminate the superconducting layer, and hence permanently damage the winding. The critical delamination stress has been found to be as low as 25 MPa in certain tapes [50].

Figure17 shows the time evolution of the of circumferential or hoop stress. The hoop stress is the highest stress component. The maximum hoop stress is at the central pancakes and of magnitude 440

MPa, and tensile in nature. This value is much less than the critical value of tensile stress found in experiments for REBCO tapes [47]. Clearly, the model is able to capture the effect of screening current on hoop stresses (see, figure 17(a-d)). In each pancake, the hoop stress is maximum at the inner radius and decreases with the radial coordinate. The top and bottom pancakes are subjected to lower stress due to screening currents. Interestingly, this trend is opposite from the radial stress.

The nature of hoop stress after discharging the magnet is of concern, especially at the top and bottom pancakes (figure 17(e)). These stresses are both tensile and compressive within each pancake leading to tensile and buckling effects at roughly the bottom and top halves of the pancake, respectively. Shunji *et al* [49] has shown such behaviour and they suggested stress modification. The success of model stem from the fact that it is able to capture such mechanics and hence it enables to take steps to diminish the forementioned effects. The hoop stress assuming no screening currents is more uniform (figure 17(f)), though there is a small variation across the magnet.

We have also calculated the axial stresses in the magnet as shown in figure 18. For most of the magnet cross section these stresses are negligible. The axial stresses in these magnet are such that it tries to topple the pancake in clockwise direction in the pancakes at the upper half of the winding and vice versa for pancakes that are on the bottom half. This phenomenon is justified as each pancake is fixed at its bottom by roller boundaries, which impose no axial displacements at that boundary ( $u_z = 0$ ). The maximum magnitude of axial stress is 110 MPa.

The shear stress is plotted in figure 19 which evolves similarly to shear strain during charging and discharging. Again, when there is no screening current the shear stress is negligible. The maximum amount of shear stress at fully charged state (see figure 19(d)) is 50 MPa. At fully discharged state, the magnet is also subjected to shear stress due to screening current induced field from the superconductor.

The effect of shear stress on REBCO superconducting tapes has not been well studied, but we could expect that tapes will be able to withstand much lower shear than hoop stresses. This is due to the brittle nature of the superconductor and the buffer layers.

### 4.2.3 Relevance of screening currents

: Next, we compare the peak quantities with and without screening currents. Figure 20 shows normalized stresses  $\bar{\sigma} = \sigma_{max}/\sigma_{scmax}$  and normalized strains  $\bar{\epsilon} = \epsilon_{max}/\epsilon_{scmax}$  for all components. The effect of screening current in amplifying the peak values is clearly demonstrated. Clearly, the screening currents increase all components of stress and strain. The strain increase is the most pronounced for the shear component, which is negligible for no screening currents but might be critical when screening currents are taken into account. The radial stress also increases substantially, by a factor 2, but the hoop stress increases by only around 10 %. , which is similar to the safety margin regarding the operating current. Then screening currents play an essential role for the shear and radial stress, but they are only relevant for the hoop stress when this component is close to the critical value.

## 4.3 Overbanding

This section discuss the effect of over banding as shown in figure 6. We consider a stiff over banding of Tungsten carbide, whose young modulus is  $650MPa$ . The thickness of overbanding layer is the same as the REBCO tape for the numerical analysis. The winding is then subjected to similar input current and external fields as in section 4.1. It is shown that using overbanding reduce the tensile stresses.

There different overbanding turns are winded on the tape and the mechanics is analyzed for the magnet. We have only shown here the effect of overbanding winding for magnet coil on radial and circumferential stresses.

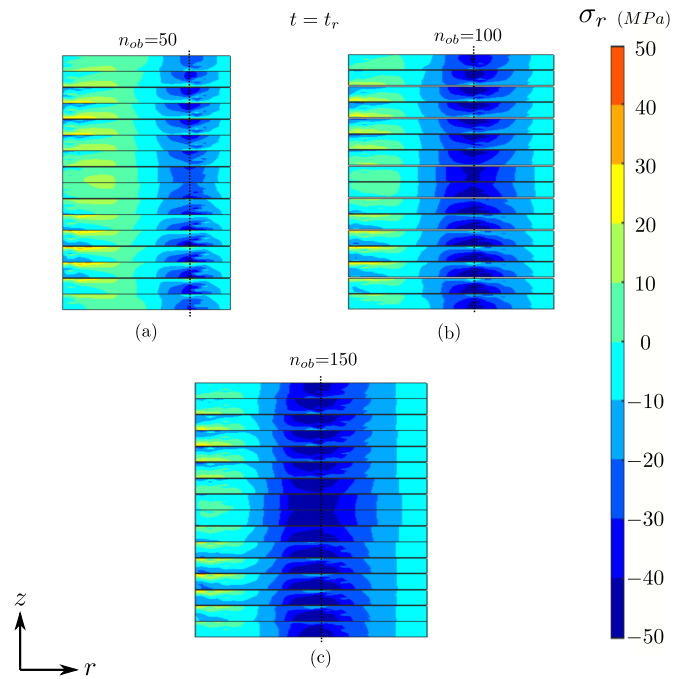


Figure 21: Variation of radial stress in the magnet subjected to screening current induced field when number of overbanding turns are (a)  $n_{ob} = 50$ , (b)  $n_{ob} = 100$  and (c)  $n_{ob} = 150$ .

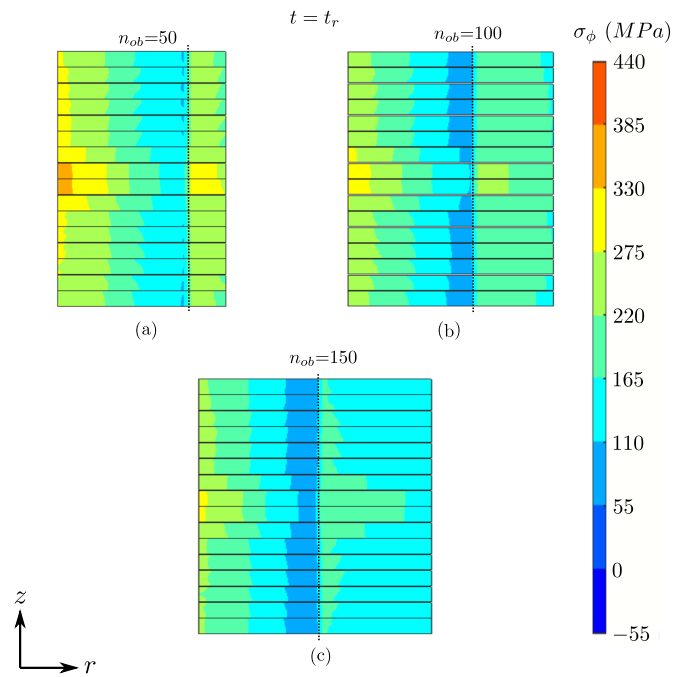


Figure 22: Variation of circumferential stress in the magnet subjected to screening current induced field when number of overbanding turns are (a)  $n_{ob} = 50$ , (b)  $n_{ob} = 100$  and (c)  $n_{ob} = 150$ .

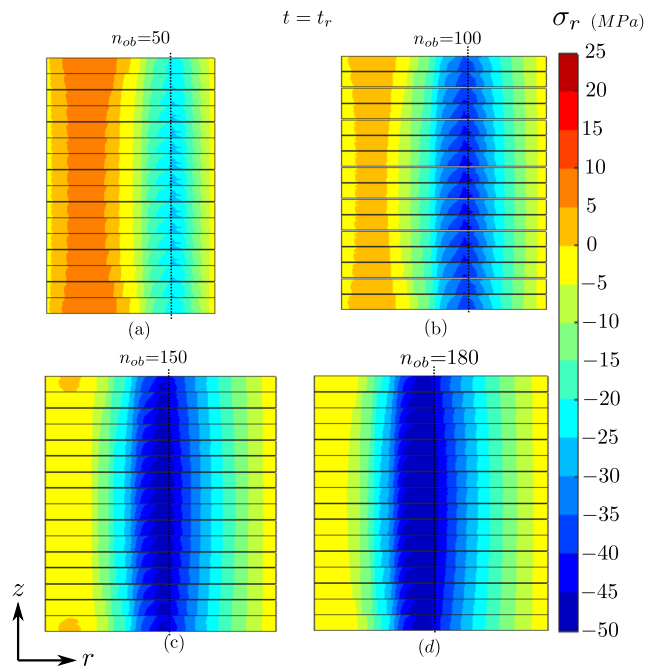


Figure 23: Variation of radial stress in the magnet subjected to no screening current induced field when number of overbanding turns are (a)  $n_{ob} = 50$ , (b)  $n_{ob} = 100$ , (c)  $n_{ob} = 150$  and (c)  $n_{ob} = 180$ .

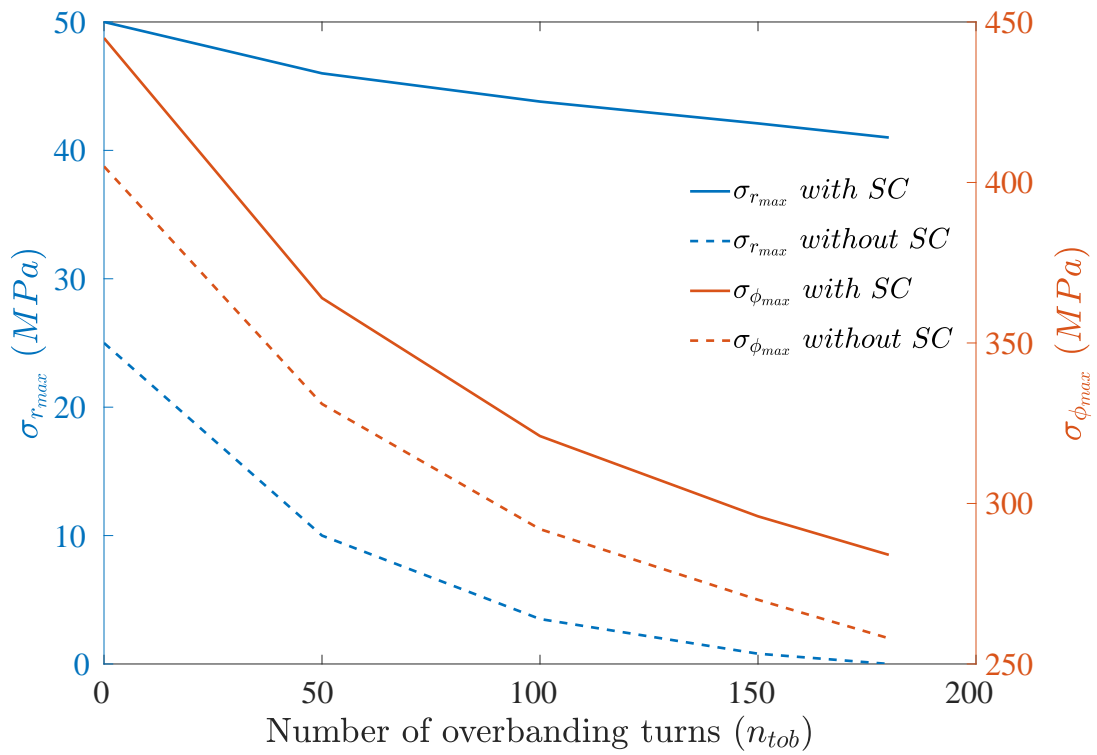


Figure 24: Variation of peak radial as well as circumferential stress with number of overbanding turns ( $n_{ob}$ ). The solid lines represents SCIF while dotted lines correspond to no SCIF.

First, we analyze the radial stress taking screening currents into account. Figure 22 shows that there is always some region with tensile stress, even for large number of turns of overbanding. However, for 100 or more turns of overbanding there is always a region within the pancake when the radial stresses are compressive for every turn of each pancake, which indicates that they are in contact with their neighbour turns. This region increases with increase in the number of overbanding turns as shown, in figure 21. In addition, the maximum stresses are reduced from 50 MPa for no overbanding to 20 MPa for  $n_{ob} = 150$ . At the boundary between the two materials the stresses are highly compressive which is reasonable because the overbanding layer acts nearly to a rigid boundary against coil expansion.

Next, we analyse the circumferential stress, which shows that this stress decreases with the number of overbanding turns (see, figure 22).

If we neglect the screening currents, the radial stresses are relatively low which are tensile in a large portion of the superconducting winding for 50 and 100 turns of overbanding, only at the top and bottom pancakes for  $n_{ob} = 150$ . The radial stress is compressive for the whole superconducting cross-section for large enough turns of overbanding (180 in our case, see, figure 23).

Finally, figure 24 shows the dependence of the peak radial and circumferential stress with the number of overbanding turns. Both peak radial and circumferential stresses are decrease with the number of overbanding turns. However, overbanding causes a higher decrease in the maximum circumferential stress than in the radial component.

## 5 Conclusions

Superconducting high field magnets are subjected to strong Lorentz forces that could damage the superconductor and other structural materials. Then, the design of high-field magnets require mechanical modelling in order to avoid damage during operation. We use this method to analyze a REBCO insert in a 32 T fully superconducting magnet. We have included the effect of screening current induced field to calculate the mechanical properties. These magnets have to function safely when subjected to high current density in order to generate highest possible magnetic field. To ensure and checking this, a fast and accurate tool is developed. Following are the salient point of the work:

1. Bulk approximation to calculate elastic properties leads to good agreement with uniaxial experiments.
2. The top and the bottom of the pancakes are more susceptible to screening currents, which cause non uniform current density and the increased strains and stresses.
3. The radial strains are compressive and maximum at the inner radius.
4. The highest component among all the strains and stresses are circumferential. Both increase with the radial coordinate.
5. The shear stresses and shear strains arise due to SCIF. Although much lower than the circumferential stress, they are a matter of concern for delamination in REBCO tapes. These mechanical quantities appear as negligible when screening currents effect are not taken into account.
6. After discharging the REBCO insert, winding is subjected to stress, which are caused by SCIF. The circumferential stress is of concern as it may lead to buckling.
7. The use of stiff overbanding material reduces the radial and circumferential stresses which protect the magnet from damage.

## Acknowledgement

A.S. acknowledges simulating discussion with Dr. Anang Dadhich at various occasion during the work. E.P. and A.S. acknowledge Oxford Instruments for providing details on the cross-section of the LTS outsert. This project has received funding from the European Union’s Horizon 2020 research and innovation programme under grant agreement No 951714 (superEMFL), and the Slovak Republic from projects APVV-19-0536 and VEGA 2/0098/24. Any dissemination of results reflects only the author’s view and the European Commission is not responsible for any use that may be made of the information it contains.

## References

- [1] Jianhua Liu, Qiuliang Wang, Lang Qin, Benzhe Zhou, Kangshuai Wang, Yaohui Wang, Lei Wang, Zili Zhang, Yinming Dai, Hui Liu, et al. World record 32.35 tesla direct-current magnetic field generated with an all-superconducting magnet. *Superconductor Science and Technology*, 33(3):03LT01, 2020.
- [2] Seungyong Hahn, Kwanglok Kim, Kwangmin Kim, Xinbo Hu, Thomas Painter, Iain Dixon, Seokho Kim, Kabindra R Bhattarai, So Noguchi, Jan Jaroszynski, et al. 45.5-tesla direct-current magnetic field generated with a high-temperature superconducting magnet. *Nature*, 570(7762):496–499, 2019.
- [3] Patrick Wikus, Wolfgang Frantz, Rainer Kümmerle, and Patrik Vonlanthen. Commercial gigahertz-class nmr magnets. *Superconductor Science and Technology*, 35(3):033001, 2022.
- [4] Y Yanagisawa, M Hamada, K Hashi, and H Maeda. Review of recent developments in ultra-high field (uhf) nmr magnets in the asia region. *Superconductor Science and Technology*, 35(4):044006, 2022.
- [5] Philippe Fazilleau, Xavier Chaud, François Debray, Thibault Lecrevisse, and Jung-Bin Song. 38 mm diameter cold bore metal-as-insulation hts insert reached 32.5 t in a background magnetic field generated by resistive magnet. *Cryogenics*, 106:103053, 2020.
- [6] Pierluigi Bruzzone, Walter H Fietz, Joseph V Minervini, Mikhail Novikov, Nagato Yanagi, Yuhu Zhai, and Jinxing Zheng. High temperature superconductors for fusion magnets. *Nuclear Fusion*, 58(10):103001, 2018.
- [7] Neil Mitchell, Jinxing Zheng, Christian Vorpahl, Valentina Corato, Charlie Sanabria, Michael Segal, Brandon Sorbom, Robert Slade, Greg Brittles, Rod Bateman, et al. Superconductors for fusion: a roadmap. *Superconductor science and technology*, 34(10):103001, 2021.
- [8] Walter H Fietz, Christian Barth, Sandra Drotziger, Wilfried Goldacker, Reinhard Heller, Sonja I Schlachter, and Klaus-Peter Weiss. Prospects of high temperature superconductors for fusion magnets and power applications. *Fusion Engineering and Design*, 88(6-8):440–445, 2013.
- [9] Lucio Rossi and Luca Bottura. Superconducting magnets for particle accelerators. *Reviews of accelerator science and technology*, 5:51–89, 2012.
- [10] P Schmuser. Superconducting magnets for particle accelerators. *Reports on Progress in Physics*, 54(5):683, 1991.



- [11] LD Cooley, AK Ghosh, and RM Scanlan. Costs of high-field superconducting strands for particle accelerator magnets. *Superconductor Science and Technology*, 18(4):R51, 2005.
- [12] Jose R Alonso and Timothy A Antaya. Superconductivity in medicine. *Reviews of Accelerator Science and Technology*, 5:227–263, 2012.
- [13] Ewald Moser, Elmar Laistler, Franz Schmitt, and Georg Kontaxis. Ultra-high field nmr and mri—the role of magnet technology to increase sensitivity and specificity. *Frontiers in Physics*, 5:33, 2017.
- [14] Yaohui Wang, Qiuliang Wang, Ming Yan, Weimin Wang, Zhifeng Chen, and Feng Liu. Passive shielding of ultra-high field mri superconducting magnet using an integral operation with nonlinear iteration. In *ISMIRM & ISMRT Annual Meeting & Exhibition 2023*, page 4235. ISMIRM, 2023.
- [15] P Vedrine, G Aubert, F Beaudet, J Belorgey, C Berriaud, P Bredy, A Donati, O Dubois, G Gilgrass, FP Juster, et al. Iseult/inumac whole body 11.7 t mri magnet status. *IEEE Transactions on Applied Superconductivity*, 20(3):696–701, 2010.
- [16] Bulent Sarlioglu and Casey T Morris. More electric aircraft: Review, challenges, and opportunities for commercial transport aircraft. *IEEE transactions on Transportation Electrification*, 1(1):54–64, 2015.
- [17] Cesar A Luongo, Philippe J Masson, Taewoo Nam, Dimitri Mavris, Hyun D Kim, Gerald V Brown, Mark Waters, and David Hall. Next generation more-electric aircraft: A potential application for hts superconductors. *IEEE Transactions on applied superconductivity*, 19(3):1055–1068, 2009.
- [18] Kiruba S Haran, Swarn Kalsi, Tabea Arndt, Haran Karmaker, Rod Badcock, Bob Buckley, Timothy Haugan, Mitsuru Izumi, David Loder, James W Bray, et al. High power density superconducting rotating machines—development status and technology roadmap. *Superconductor Science and Technology*, 30(12):123002, 2017.
- [19] Francesco Grilli, Tara Benkel, Jens Hänisch, Mayraluna Lao, Thomas Reis, Eva Berberich, Simon Wolfstädter, Christian Schneider, Paul Miller, Chloe Palmer, et al. Superconducting motors for aircraft propulsion: The advanced superconducting motor experimental demonstrator project. In *Journal of Physics: Conference Series*, volume 1590, page 012051. IOP Publishing, 2020.
- [20] Salama, V Selvamanickam, L Gao, and K Sun. High current density in bulk  $yba_2cu_3o_x$  superconductor. *Applied Physics Letters*, 54(23):2352–2354, 1989.
- [21] Shijie Shi and Rui Liang. Numerical analysis of rebco high-temperature superconducting (hts) coils based on screening effect. *Journal of Superconductivity and Novel Magnetism*, 35(12):3487–3496, 2022.
- [22] H Miyazaki, S Iwai, T Tosaka, K Tasaki, and Y Ishii. Delamination strengths of different types of rebco-coated conductors and method for reducing radial thermal stresses of impregnated rebco pancake coils. *IEEE Transactions on Applied Superconductivity*, 25(3):1–5, 2015.
- [23] Vincent Arp. Stresses in superconducting solenoids. *Journal of Applied Physics*, 48(5):2026–2036, 1977.
- [24] Martin N Wilson. Superconducting magnets, clarendon, 1983.

- [25] WH Gray and JK Ballou. Electromechanical stress analysis of transversely isotropic solenoids. *Journal of Applied Physics*, 48(7):3100–3109, 1977.
- [26] Mengdie Niu, Jing Xia, and Huadong Yong. Numerical analysis of the electromechanical behavior of high-field rebco coils in all-superconducting magnets. *Superconductor Science and Technology*, 34(11):115005, 2021.
- [27] Xudong Wang, Yoshiaki Tsuji, Atsushi Ishiyama, Hiroshi Yamakawa, Tomonori Watanabe, and Shigeo Nagaya. Experiment and numerical analysis on the yoroi structure for high-strength rebco coil. *IEEE Transactions on Applied Superconductivity*, 26(4):1–4, 2016.
- [28] Hiroshi Ueda, Hideaki Maeda, Yu Suetomi, and Yoshinori Yanagisawa. Experiment and numerical simulation of the combined effect of winding, cool-down, and screening current induced stresses in rebco coils. *Superconductor Science and Technology*, 35(5):054001, 2022.
- [29] Frederic Trillaud, Edgar Berrospe-Juarez, Víctor MR Zermeño, and Francesco Grilli. Electromagneto-mechanical model of high temperature superconductor insert magnets in ultra high magnetic fields. *Superconductor Science and Technology*, 35(5):054002, 2022.
- [30] Ze Jing. Numerical modelling and simulations on the mechanical failure of bulk superconductors during magnetization: based on the phase-field method. *Superconductor Science and Technology*, 33(7):075009, 2020.
- [31] Wei Pi, Shuwen Ma, Yanqing Lu, Yuantong Ma, Yinshun Wang, Qingmei Shi, and Jin Dong. Strain analysis and bending properties of quasi-isotropic superconducting strand based on laminate theory. *Fusion Engineering and Design*, 162:112110, 2021.
- [32] Jing Xia, Hongyu Bai, Huadong Yong, Hubertus W Weijers, Thomas A Painter, and Mark D Bird. Stress and strain analysis of a rebco high field coil based on the distribution of shielding current. *Superconductor Science and Technology*, 32(9):095005, 2019.
- [33] Peifeng Gao, Wan-Kan Chan, Xingzhe Wang, Youhe Zhou, and Justin Schwartz. Stress, strain and electromechanical analyses of (re) ba2cu3ox conductors using three-dimensional/two-dimensional mixed-dimensional modeling: fabrication, cooling and tensile behavior. *Superconductor Science and Technology*, 33(4):044015, 2020.
- [34] Xudong Wang, Hirotaka Umeda, Atsushi Ishiyama, Masaki Tashiro, Hiroshi Yamakawa, Hiroshi Ueda, Tomonori Watanabe, and Shigeo Nagaya. Development of non-circular rebco pancake coil for high-temperature superconducting cyclotron. *IEEE Transactions on Applied Superconductivity*, 25(3):1–4, 2014.
- [35] Enric Pardo. Modeling of screening currents in coated conductor magnets containing up to 40000 turns. *Superconductor Science and Technology*, 29(8):085004, 2016.
- [36] Xiaorong Wang, Stephen A Gourlay, and Soren O Prestemon. Dipole magnets above 20 tesla: Research needs for a path via high-temperature superconducting rebco conductors. *Instruments*, 3(4):62, 2019.
- [37] Hideaki Maeda and Yoshinori Yanagisawa. Recent developments in high-temperature superconducting magnet technology. *IEEE Transactions on applied superconductivity*, 24(3):1–12, 2013.

- [38] Yufan Yan, Peng Song, Canjie Xin, Mingzhi Guan, Yi Li, HuaJun Liu, and Timing Qu. Screening-current-induced mechanical strains in rebco insert coils. *Superconductor Science and Technology*, 34(8):085012, 2021.
- [39] C Barth, N Bagrets, KP Weiss, CM Bayer, and T Bast. Degradation free epoxy impregnation of rebco coils and cables. *Superconductor Science and Technology*, 26(5):055007, 2013.
- [40] Essia Hannachi and Yassine Slimani. Mechanical properties of superconducting materials. In *Superconducting Materials: Fundamentals, Synthesis and Applications*, pages 89–121. Springer, 2022.
- [41] Enric Pardo, Ján Šouc, and Lubomir Frolek. Electromagnetic modelling of superconductors with a smooth current–voltage relation: variational principle and coils from a few turns to large magnets. *Superconductor Science and Technology*, 28(4):044003, 2015.
- [42] A Patel, SC Hopkins, A Baskys, V Kalitka, A Molodyk, and BA Glowacki. Magnetic levitation using high temperature superconducting pancake coils as composite bulk cylinders. *Superconductor Science and Technology*, 28(11):115007, 2015.
- [43] E Pardo and P Fazilleau. Fast and accurate electromagnetic modeling of non-insulated and metal-insulated REBCO magnets. 2023. arXiv:2309.02249.
- [44] Jerome Fleiter and Amalia Ballarino. Parameterization of the critical surface of REBCO conductors from Fujikura. *CERN internal note, EDMS*, 1426239, 2014.
- [45] Allan F Bower. *Applied mechanics of solids*. CRC press, 2009.
- [46] Hubertus W Weijers, W Denis Markiewicz, Andrew V Gavrilin, Adam J Voran, Youri L Viouchkov, Scott R Gundlach, Patrick D Noyes, Dima V Abraimov, Hongyu Bai, Scott T Hannahs, et al. Progress in the development and construction of a 32-t superconducting magnet. *IEEE Transactions on Applied Superconductivity*, 26(4):1–7, 2016.
- [47] Christian Barth, Giorgio Mondonico, and Carmine Senatore. Electro-mechanical properties of rebco coated conductors from various industrial manufacturers at 77 k, self-field and 4.2 k, 19 t. *Superconductor Science and Technology*, 28(4):045011, 2015.
- [48] David V Hutton. *Fundamentals of finite element analysis*. The McGraw Hill Companies., 2004.
- [49] Shunji Takahashi, Yu Suetomi, Tomoaki Takao, Yoshinori Yanagisawa, Hideaki Maeda, Yasuaki Takeda, and Jun-ichi Shimoyama. Hoop stress modification, stress hysteresis and degradation of a rebco coil due to the screening current under external magnetic field cycling. *IEEE Transactions on Applied Superconductivity*, 30(4):1–7, 2020.
- [50] Daniel C van der Laan, JW Ekin, Cameron C Clickner, and Theodore C Stauffer. Delamination strength of ybco coated conductors under transverse tensile stress. *Superconductor Science and Technology*, 20(8):765, 2007.